Science Advances
AAAS

advances.sciencemag.org/cgi/content/full/7/1/eabd4639/DC1

Supplementary Materials for

Soft implantable drug delivery device integrated wirelessly with wearable devices to treat fatal seizures

Hyunwoo Joo, Youngsik Lee, Jaemin Kim, Jeong-Suk Yoo, Seungwon Yoo, Sangyeon Kim, Ashwini Kumar Arya, Sangjun Kim, Seung Hong Choi, Nanshu Lu, Han Sang Lee, Sanghoek Kim*, Soon-Tae Lee*, Dae-Hyeong Kim*

*Corresponding author. Email: dkim98@snu.ac.kr (D.-H.K.); staelee@snu.ac.kr (S.-T.L.); sanghoek@khu.ac.kr (Sanghoek Kim)

Published 1 January 2021, *Sci. Adv.* **7**, eabd4639 (2021)
DOI: 10.1126/sciadv.abd4639

The PDF file includes:

Figs. S1 to S20
Legends for movies S1 and S2
Supplementary Texts S1 to S4
References

Other Supplementary Material for this manuscript includes the following:

(available at advances.sciencemag.org/cgi/content/full/7/1/eabd4639/DC1)

Movies S1 and S2
Supplementary Software ZIP File

SUPPLEMENTARY FIGURES

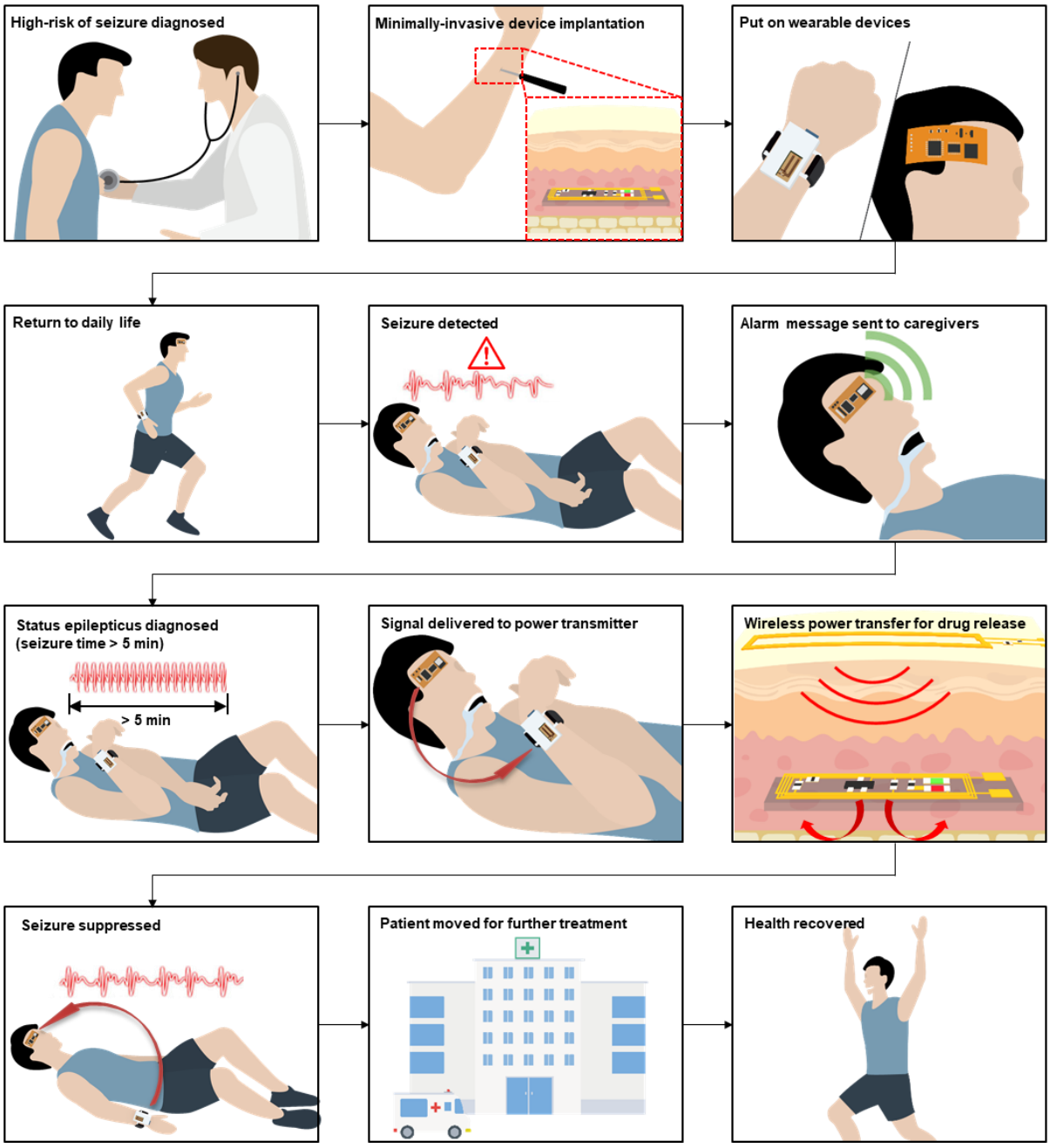

Fig. S1. Point-of-care treatment scenario of the fatal epileptic medical emergency by using the SID. Schematic illustrations of the scenario in which the SID is implanted subcutaneously and wearable devices are put onto a patient for point-of-care treatment based on continuous health monitoring. The loaded drug is subcutaneously released in case of fatal epileptic medical emergencies such as status epilepticus.

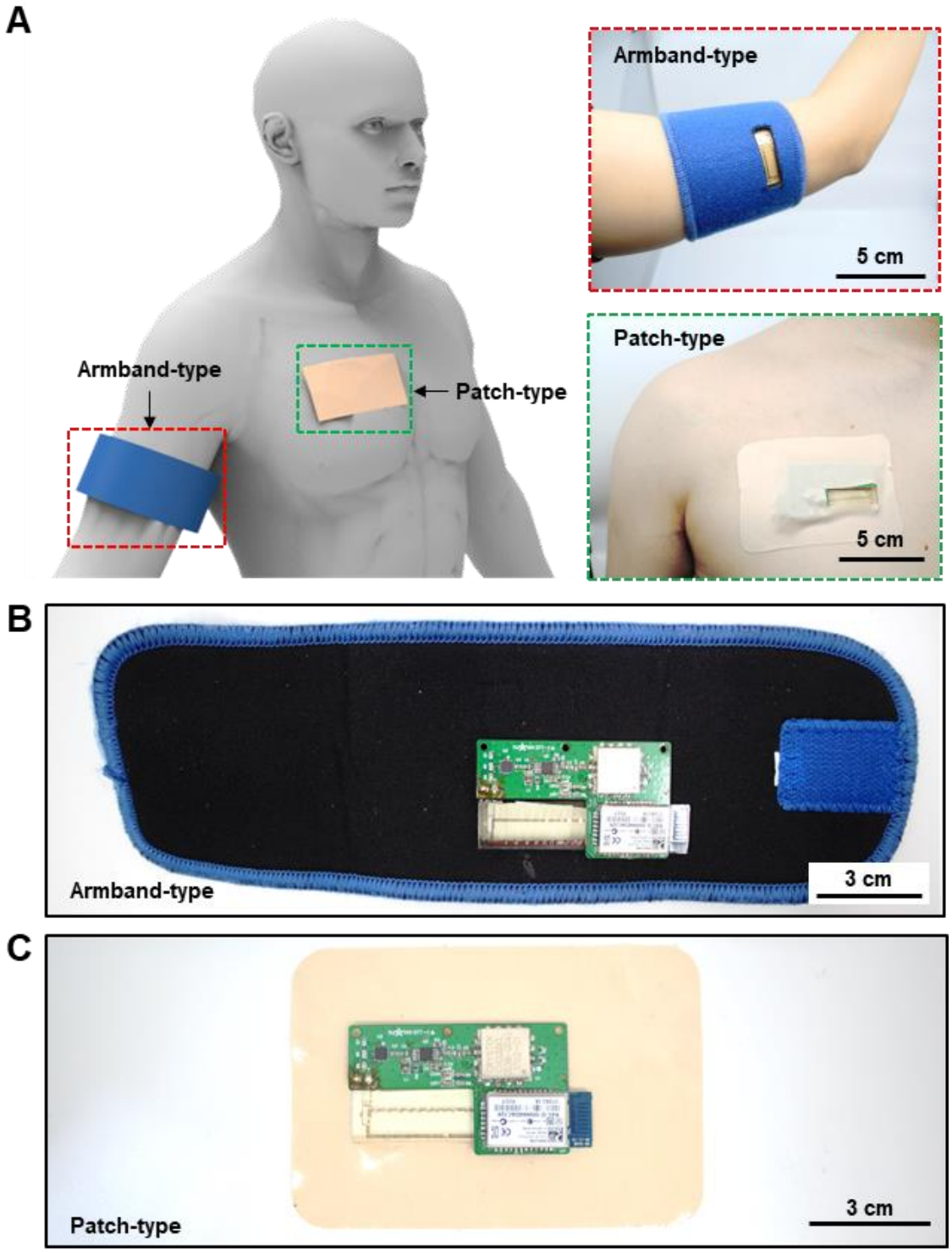

Fig. S2. Various types of wearable power transmitters depending on the location of SID. (**A**) Schematic illustration and images of various types of wearable power transmitters such as an armband-type (red dotted box) or a patch-type (green dotted box) device. (**B**) Photo that shows the inside of the armband-type power transmitter. (**C**) Photo that shows the inside of the patch-type power transmitter. Photo credit: Hyunwoo Joo, Seoul National University.

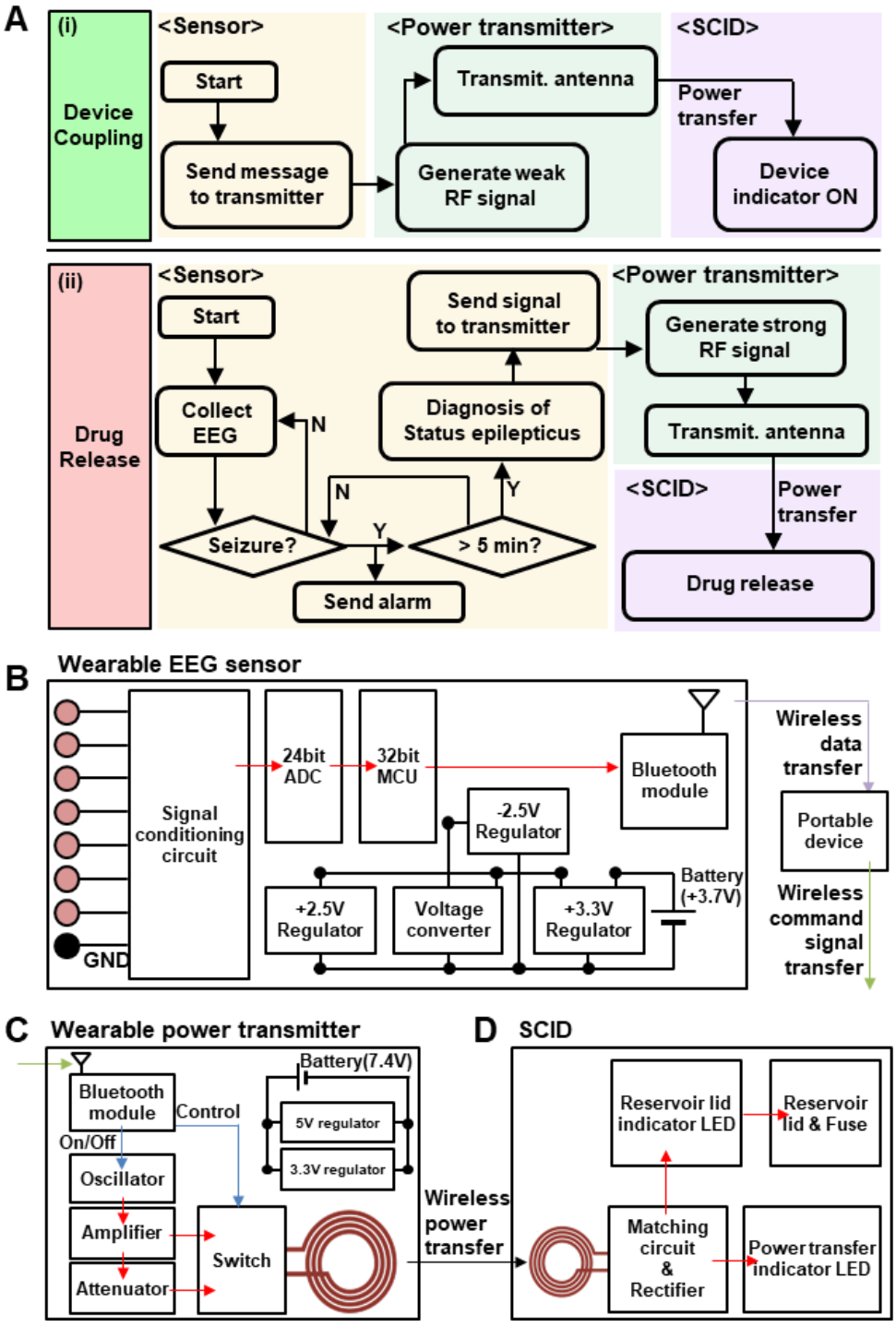

Fig. S3. Flow chart and block diagram showing the overall system construction and operation. (**A**) Flow chart for the (i) wireless device coupling and (ii) drug release process. (**B**) Block diagram of the wearable EEG sensor showing the construction of its main circuit components. (**C**) Block diagram of the wearable power transmitter showing the construction of its main circuit components. (**D**) Block diagram of the SID showing the construction of its main circuit components.

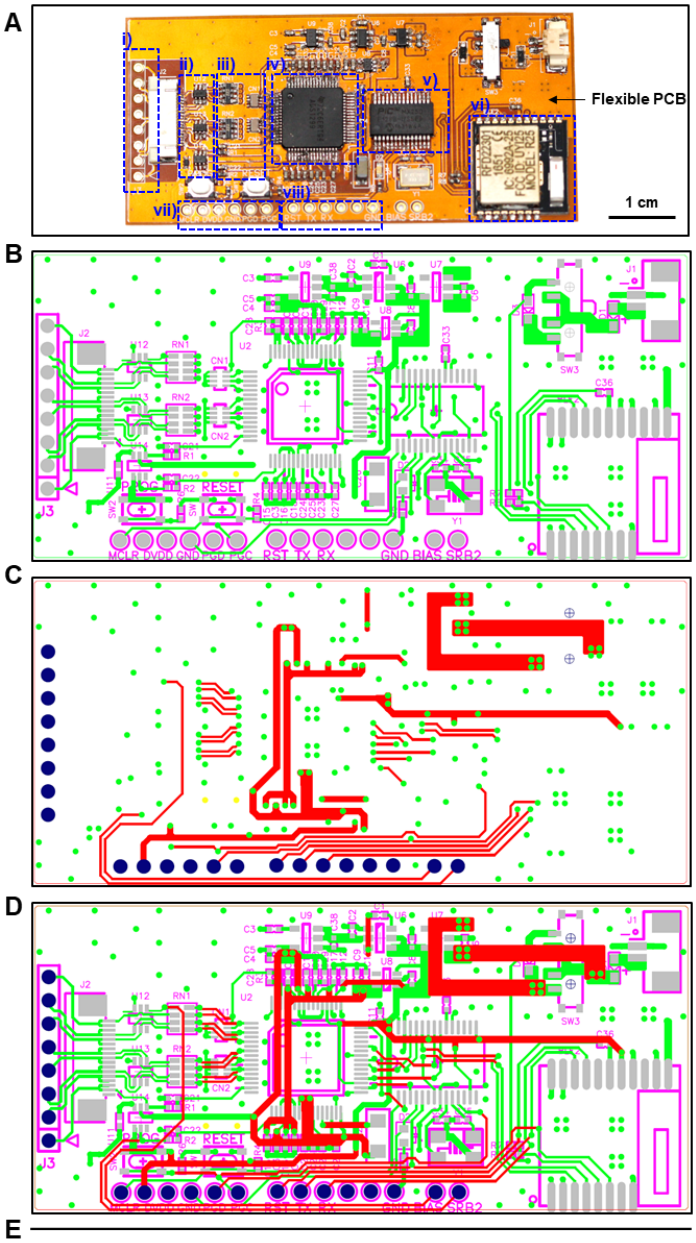

E

Category	Manufacturer	Manufacturer Part #
Analog-to-digital converter	Texas Instruments	ADS1299IPAGR
Microcontroller unit	Microchip Technology	PIC32MX250F128B-I/SS
Bluetooth module	RF Digital	RFduino 22301
3.3V regulator	Texas Instruments	LP5907QMFX-3.3Q1
2.5V regulator	Texas Instruments	TLV70025DCKR
-2.5V regulator	Texas Instruments	TPS72325DBVR
Voltage converter	Texas Instruments	LM2664M6/NOPB

Fig. S4. Circuit design and information of microchips for the wearable sensor. (**A**) Image of the wearable EEG sensor. (**B-D**) Circuit layout on the flexible PCB for the wearable EEG senor. (**E**) List of the chipsets used for the circuit construction. Photo credit: Hyunwoo Joo, Seoul National University.

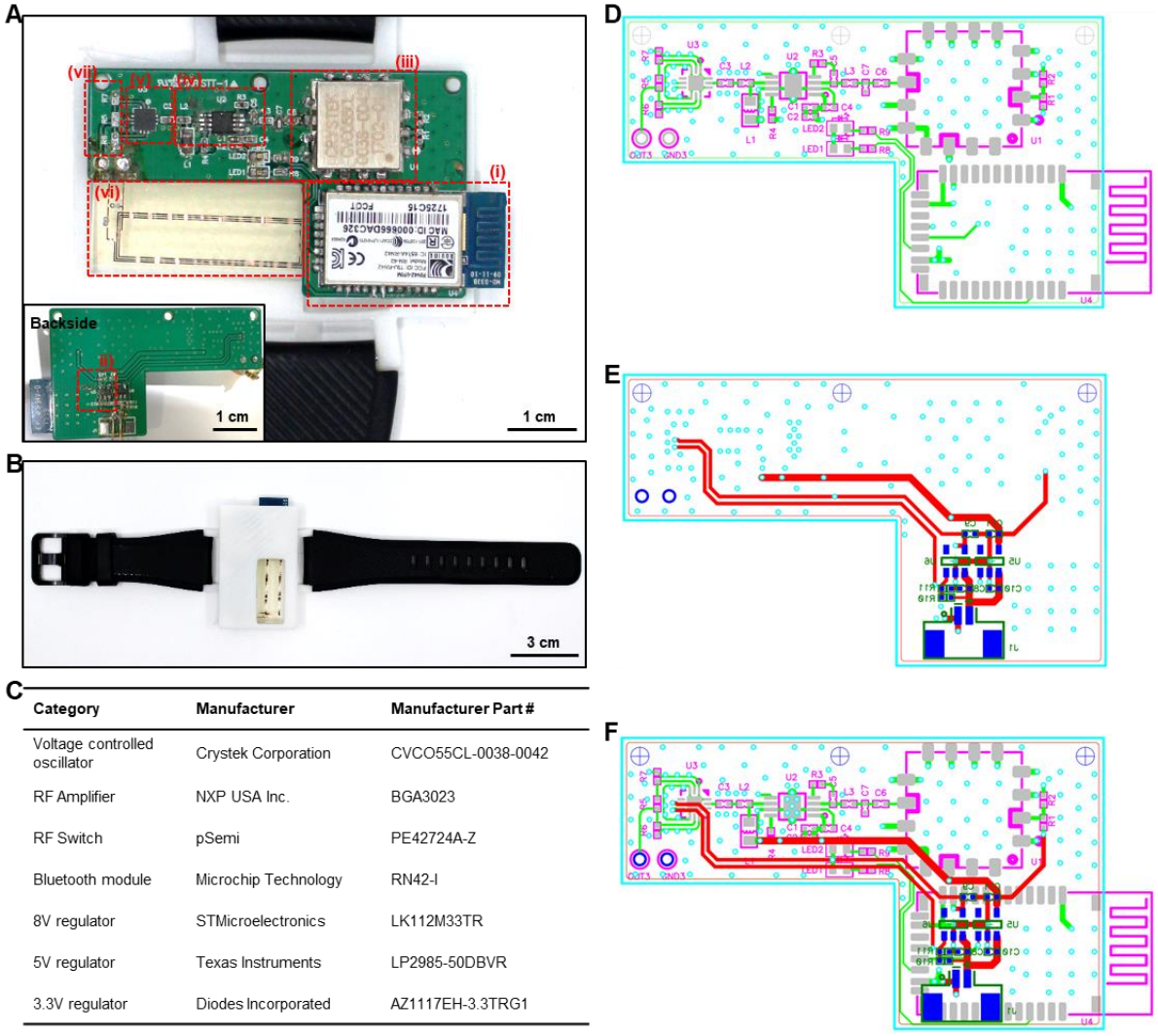

Category	Manufacturer	Manufacturer Part #
Voltage controlled oscillator	Crystek Corporation	CVCO55CL-0038-0042
RF Amplifier	NXP USA Inc.	BGA3023
RF Switch	pSemi	PE42724A-Z
Bluetooth module	Microchip Technology	RN42-I
8V regulator	STMicroelectronics	LK112M33TR
5V regulator	Texas Instruments	LP2985-50DBVR
3.3V regulator	Diodes Incorporated	AZ1117EH-3.3TRG1

Fig. S5. Circuit design and information of microchips for the wearable power transmitter. (**A**) Image of the watch-type wearable power transmitter. (**B**) Image of the wearable power transmitter assembled in the housing. (**C**) List of the chipsets used for the circuit construction. (**D-F**) Circuit layout on the PCB for the wearable power transmitter. Photo credit: Hyunwoo Joo, Seoul National University.

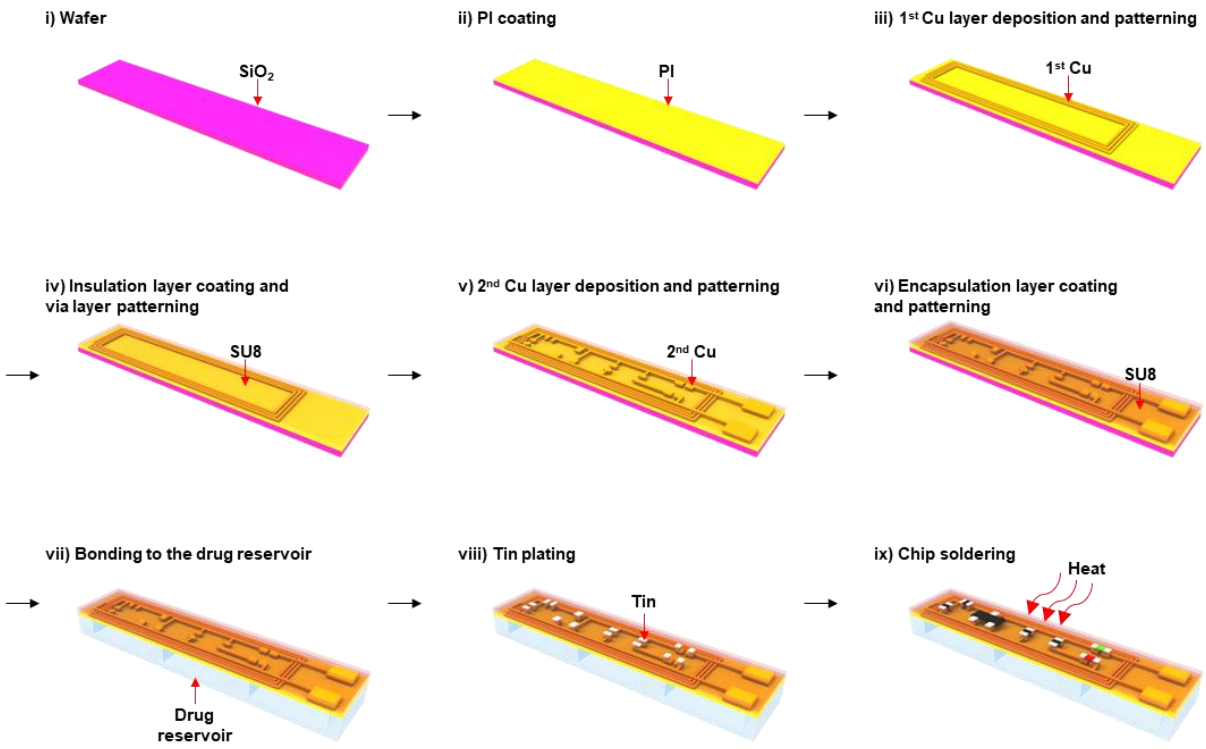

Fig. S6. Fabrication of the front side of the SID. Step-by-step illustration for the front side of the SID fabrication procedures such as the antenna fabrication, bonding with the drug reservoir, and chip soldering. Fabrication of the drug reservoir is described in Methods.

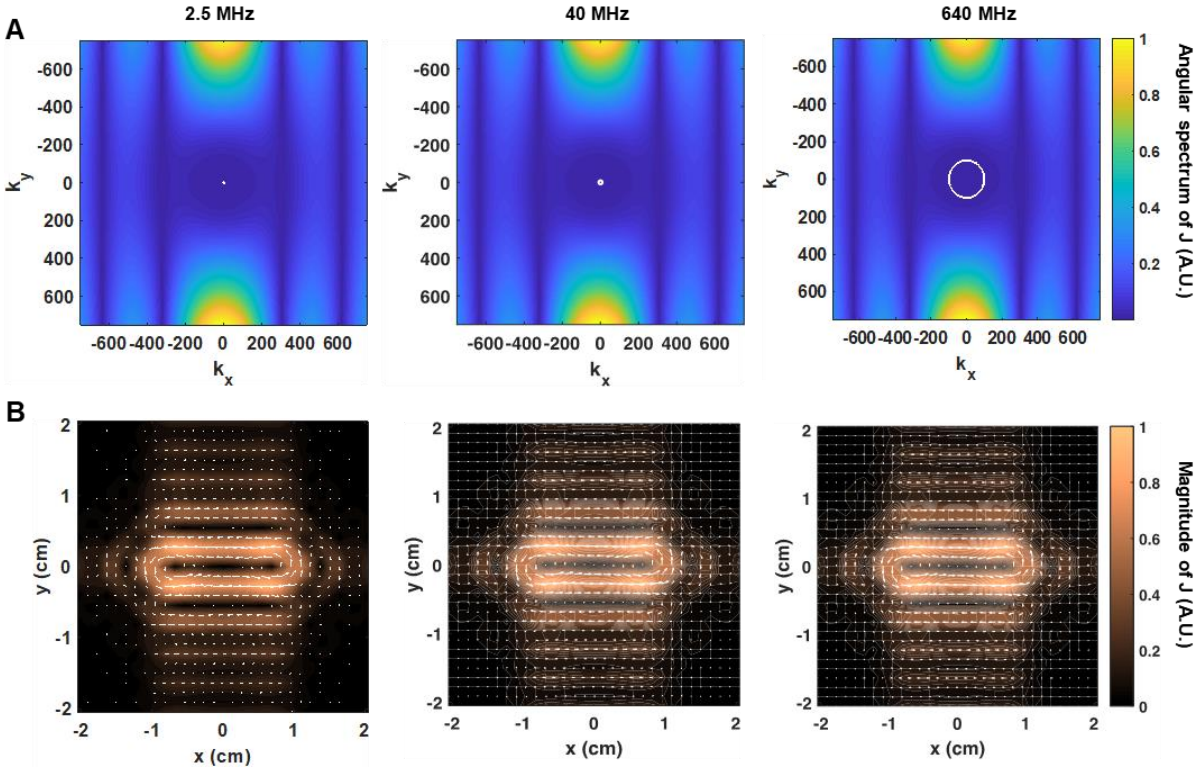

Fig. S7. Optimal electric current density. (**A**) Angular spectrums of the optimal current under the operating frequency of 2.5, 40, and 640 MHz. (**B**) Spatial distributions of the optimal current under the operation frequency of 2.5, 40, and 640 MHz.

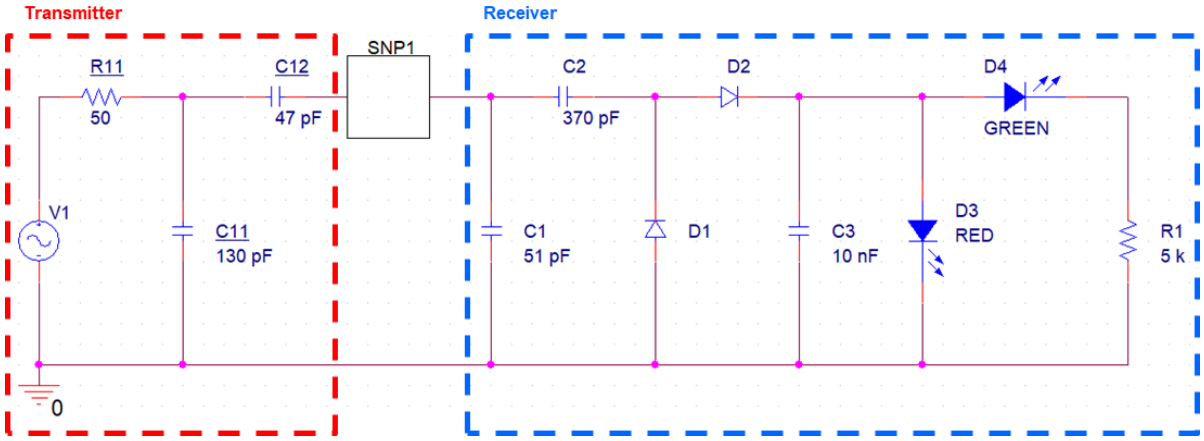

Fig. S8. Schematic diagram of the transmitter and receiver. The values of the matching capacitors (Transmitter: C11, C12, Receiver: C1, C2) are finely adjusted through the experiment to achieve minimum reflection coefficient (S_{11}) at 40 MHz.

A

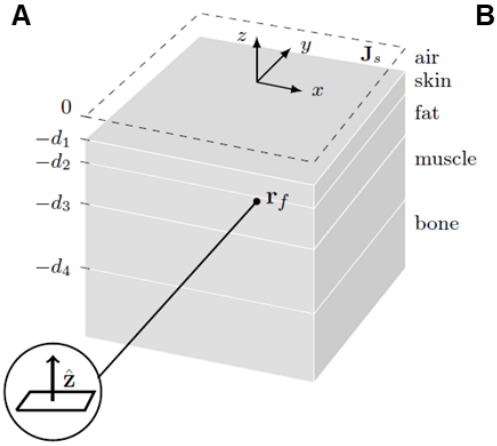

B

Medium	Thickness (mm)	Relative permittivity	Conductivity (S/m)
Air	1	1	0
Skin	1	124	0.38
Fat	2	15.4	0.064
Muscle	13	82.6	0.67
Bone	15	35.9	0.15

Fig. S9. Layered tissue model. (**A**) Multilayer tissue model used for the numerical simulation. (**B**) Nominal thickness, relative permittivity, and conductivity of each medium in the model at the operating frequency of 40 MHz.

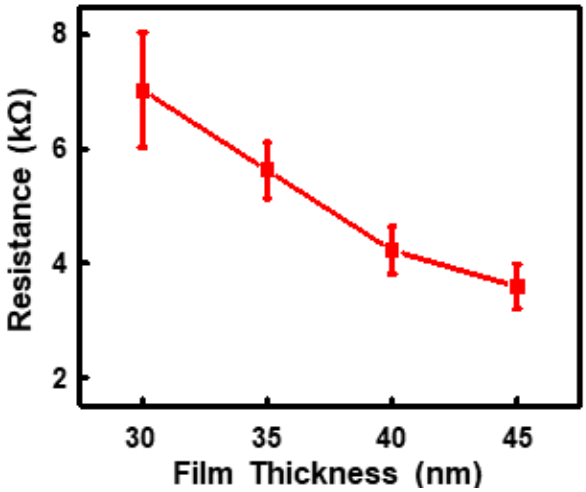

Fig. S10. Lid resistance change depending on film thickness. Measurement results of the lid resistance when the thickness of the fuse layer changes from 30 to 45 nm.

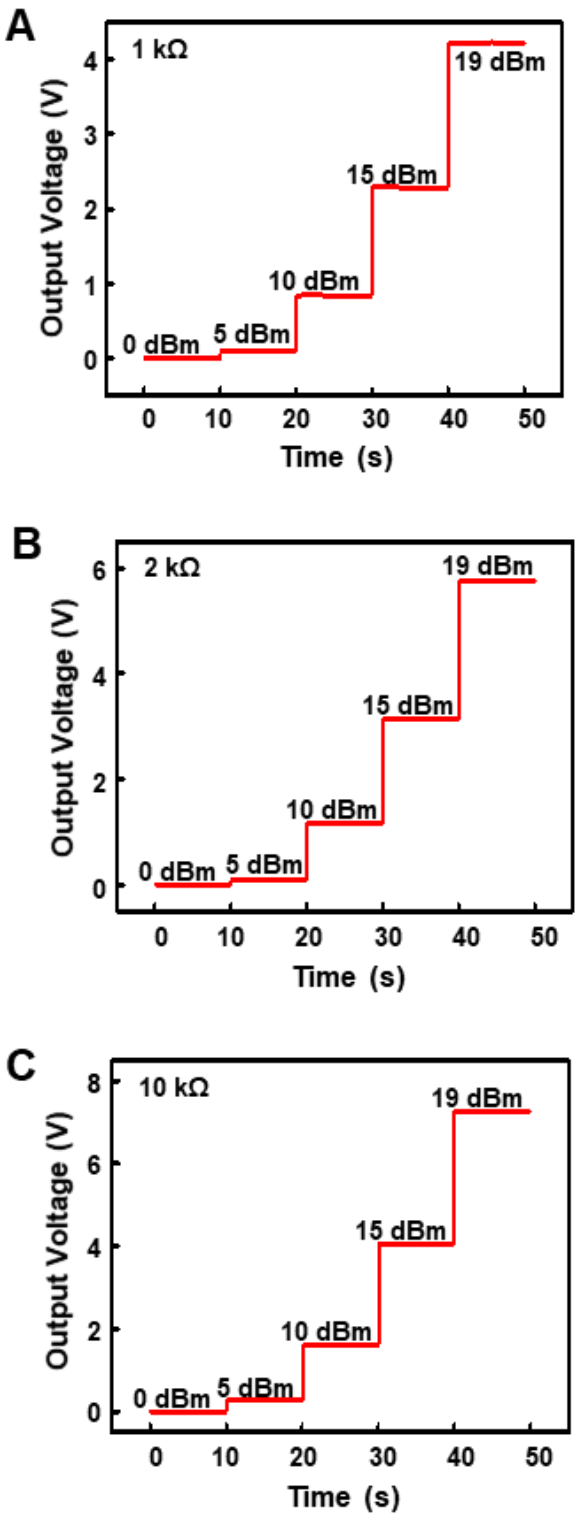

Fig. S11. Output voltage depending on the lid resistance. Output voltage measured with various input powers when the lid resistance is (**A**) 1 kΩ, (**B**) 2 kΩ, and (**C**) 10 kΩ.

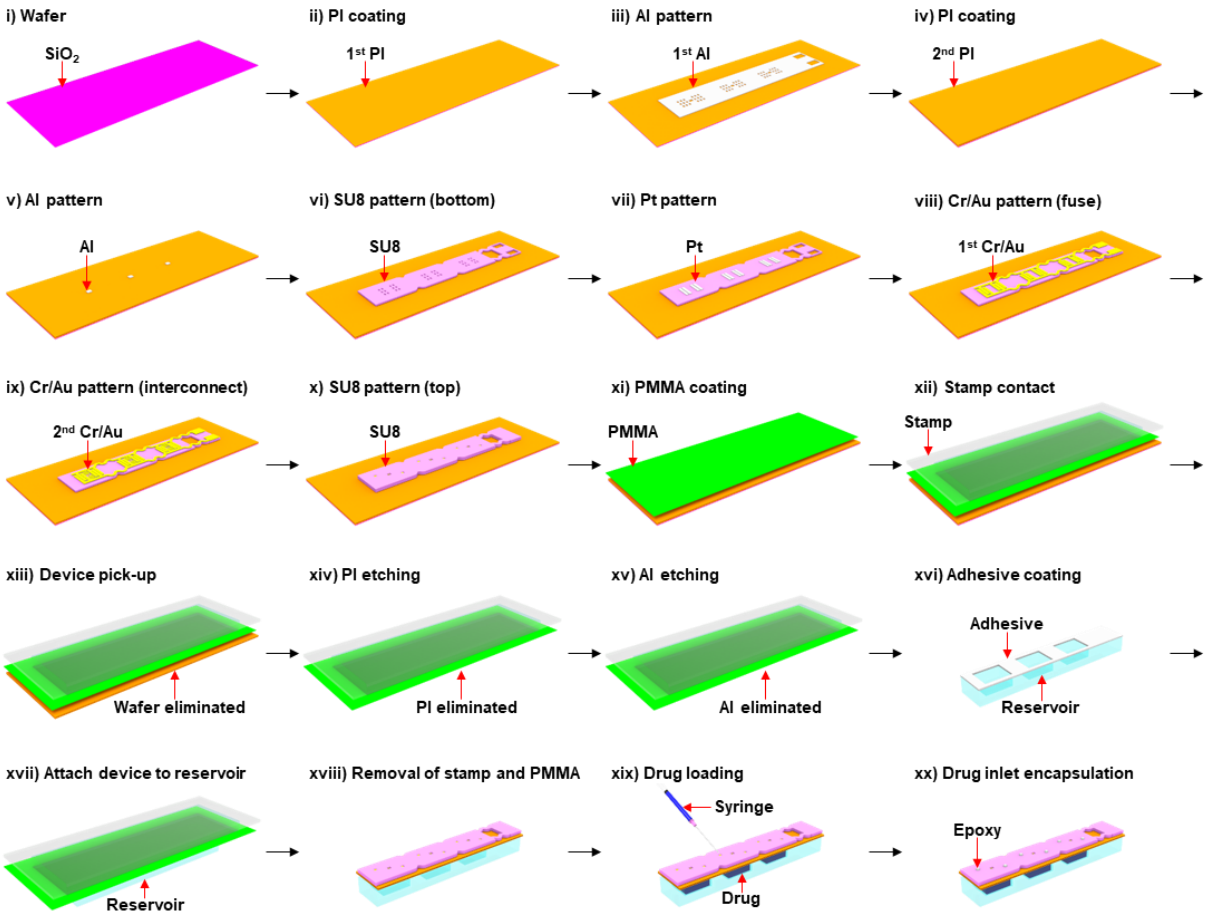

Fig. S12. Fabrication process of the backside of the SID. Step-by-step illustration of fabrication procedures for the backside of the SID such as the lid fabrication and drug injection.

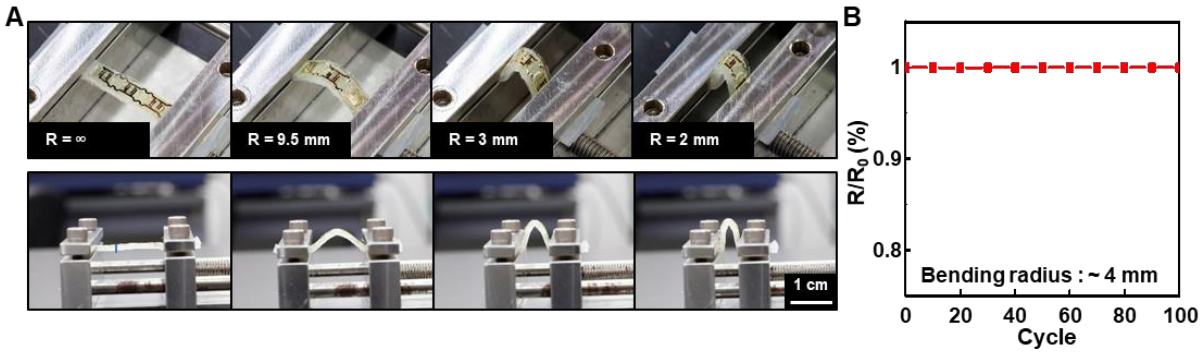

Fig. S13. Mechanical stability of the SID under bending. (**A**) Images (top and side view) of bending experiments of the SID. (**B**) Resistance change of the lid of the SID under 100 bending tests. No resistance increase was observed, which confirms that there was no mechanical damage to the device. Photo credit: Hyunwoo Joo, Seoul National University.

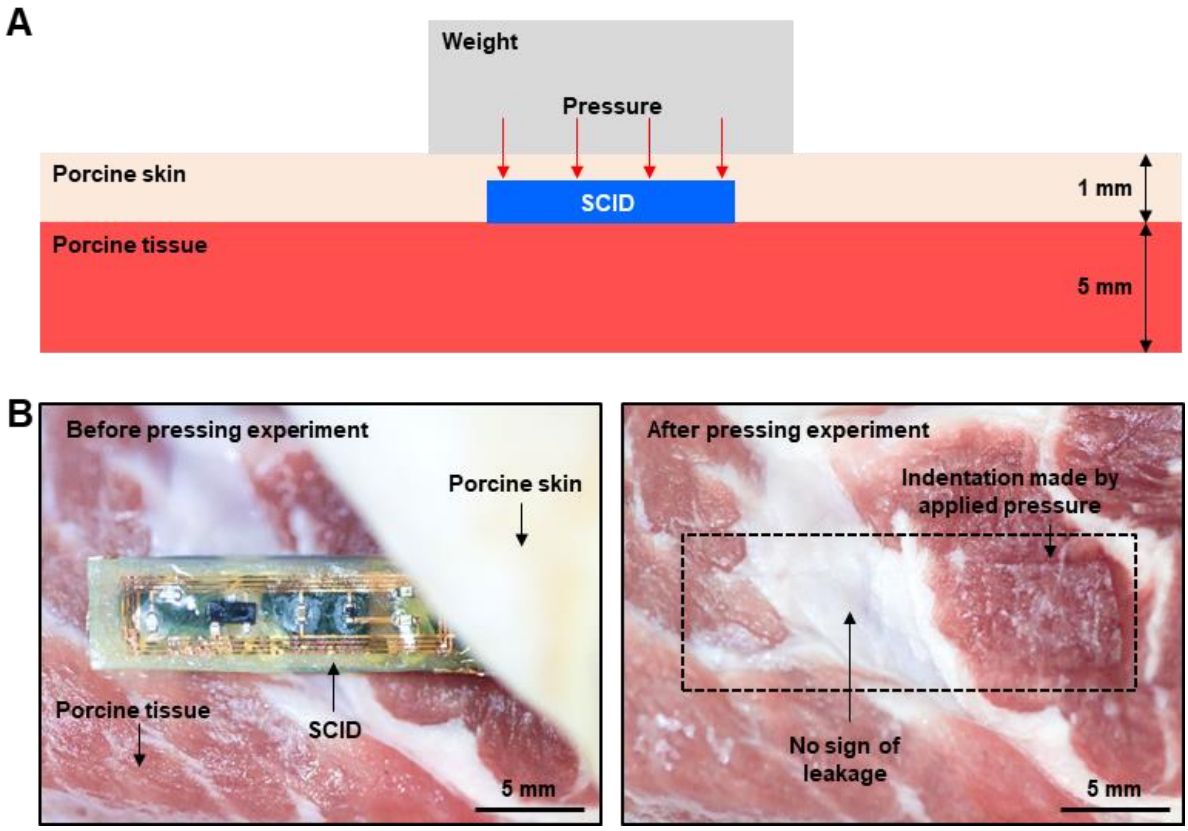

Fig. S14. Mechanical stability of SID under vertical pressure. (**A**) Schematic illustration of the experimental setting for the mechanical pressing test. The SID containing a model drug (Evans blue; for visualization) was placed on the porcine tissue and covered by the porcine skin, on which a weight (i.e., pressure) was applied. (**B**) Images before and after the mechanical pressing experiment. No sign of drug leakage was observed up to ~20 kPa of the applied pressure. Photo credit: Hyunwoo Joo, Seoul National University.

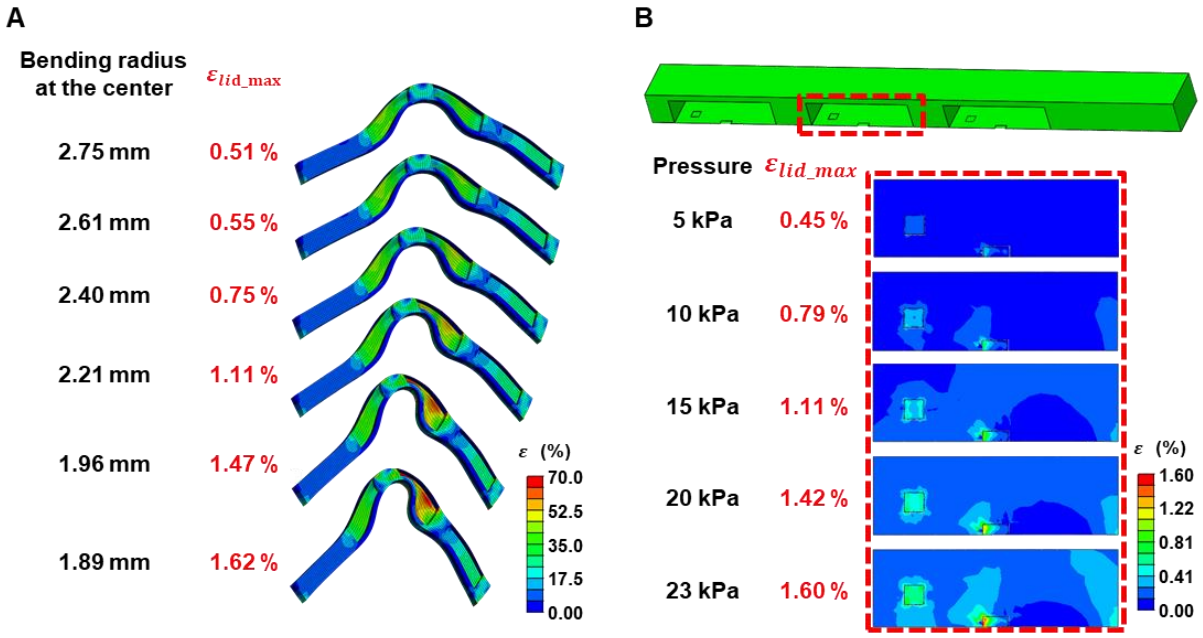

Fig. S15. Strain distribution analysis across SID under mechanical deformations. (**A**) FEA result of strain distribution across the SID under bending. (**B**) FEA result of strain distribution across the vertically pressed SID embedded under 1 mm thick skin.

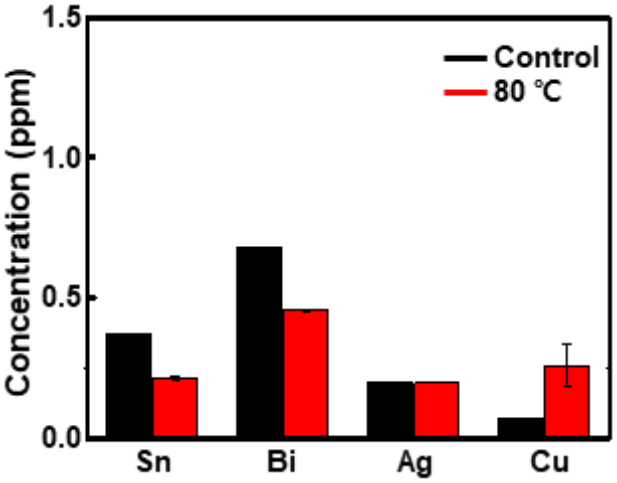

Fig. S16. Concentration of eluted metal ions from SID. ICPS results of the eluted metal ions (Sn, Bi, Ag, and Cu) from the SID during 5 days of accelerated test at 80 ℃

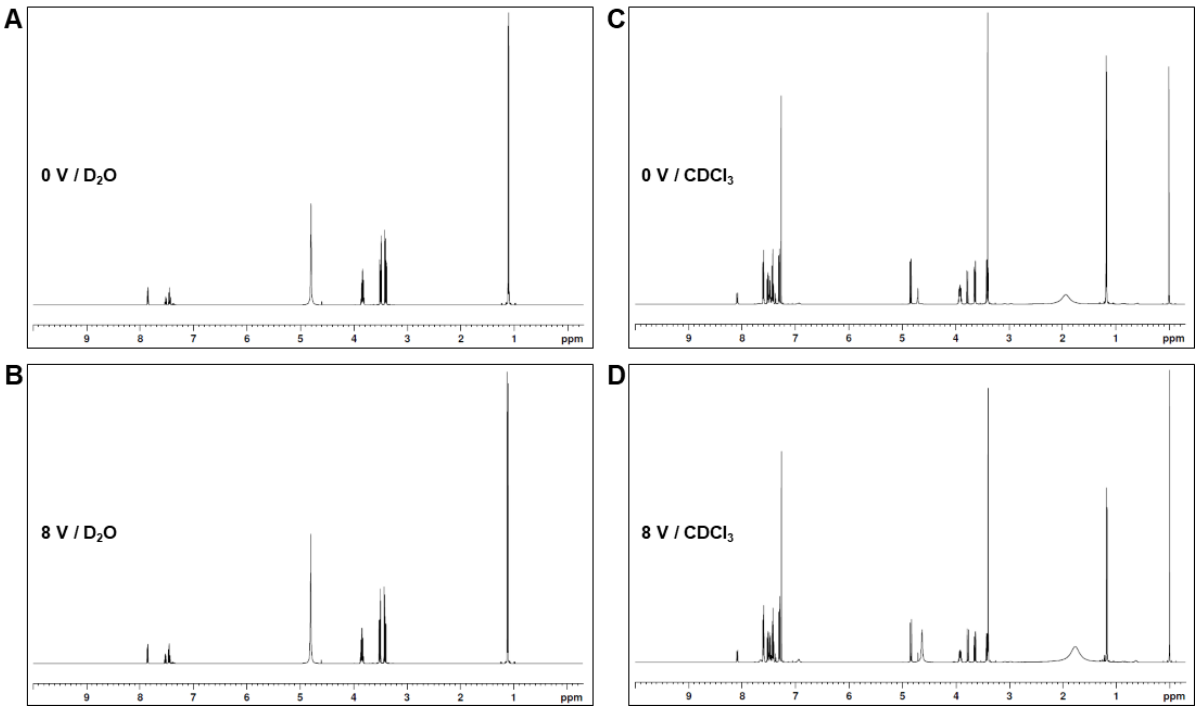

Fig. S17. ^{1}H NMR spectroscopy of diazepam before and after electrolysis. (**A and B**) ^{1}H NMR spectroscopy of diazepam (**A**) before and (**B**) after electrolysis. The samples were dissolved in D_2O. (**C and D**) ^{1}H NMR spectroscopy of diazepam (**C**) before and (**D**) after electrolysis. Extracts that were not dissolved in D_2O were collected and dissolved in $CDCl_3$.

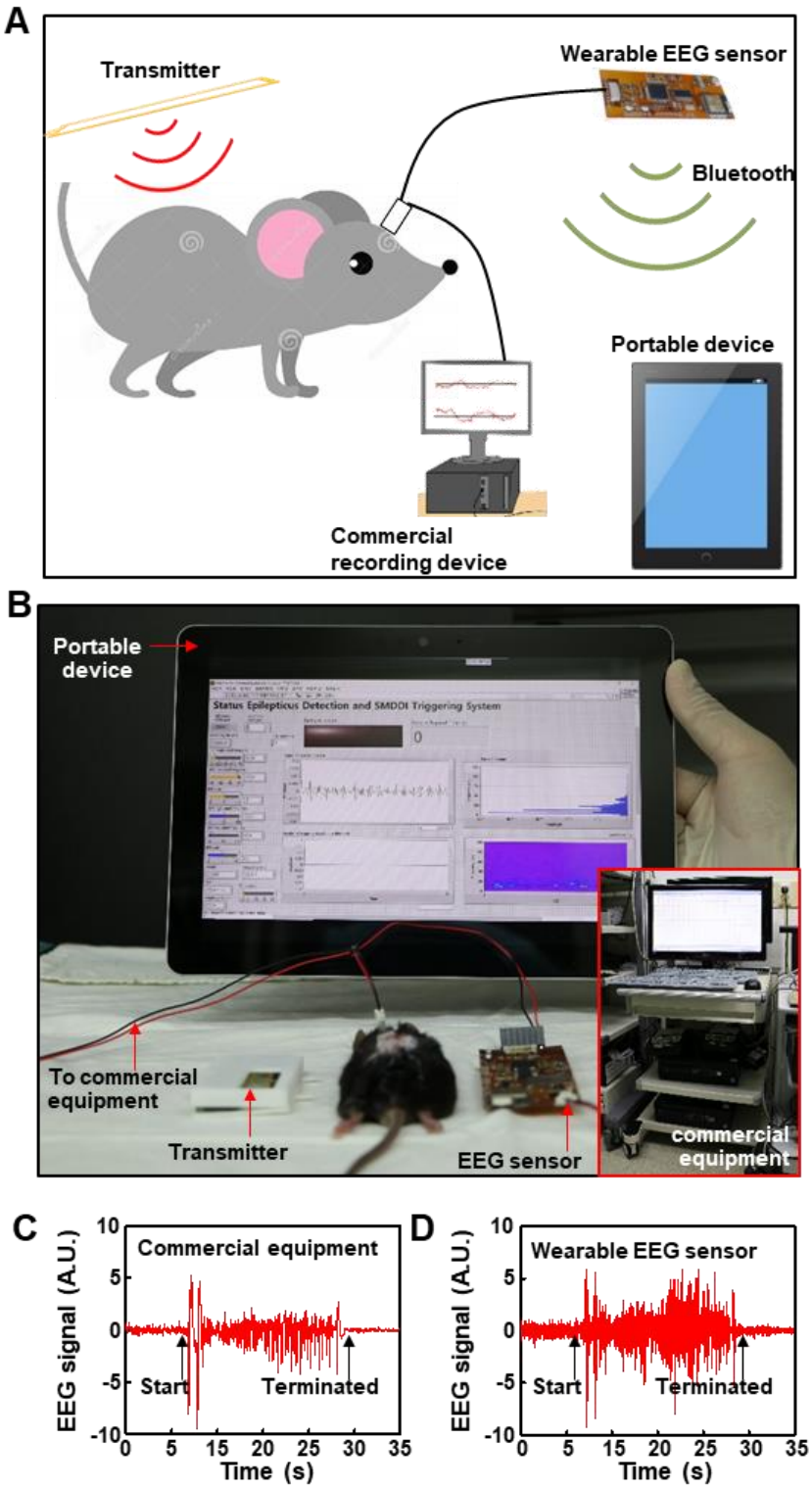

Fig. S18. In vivo animal experiment set-up and the recorded EEG signals. (**A)** Schematic illustration of the in vivo animal experiment set-up. (**B**) Image of the in vivo animal experiment set-up. (**C**) Seizure signals from the subject mouse monitored by the commercial equipment. (**D**) Seizure signals from the subject mouse monitored by the wearable EEG sensor. Photo credit: Hyunwoo Joo, Seoul National University.

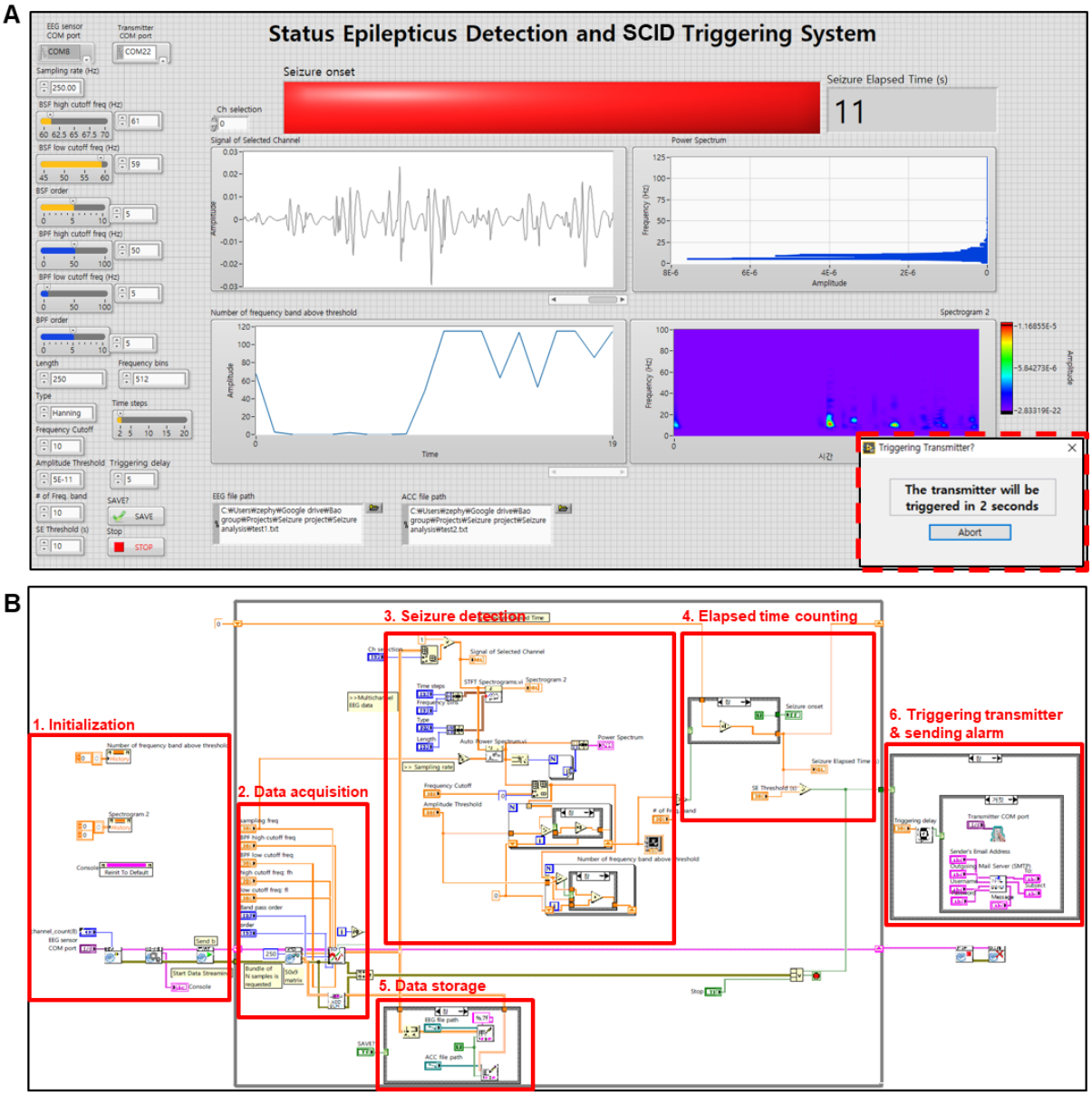

Fig. S19. Front panel and source code of the custom-made software. (**A**) Front panel of the software displaying the real-time EEG signal, frequency analysis results, alarm for the seizure onset, and elapsed time of the seizure. The right-bottom inset shows a dialogue window to the user for the notice of the wireless triggering of the drug release from the SID. (**B**) Block diagram (source codes) of the software written by LabVIEW.

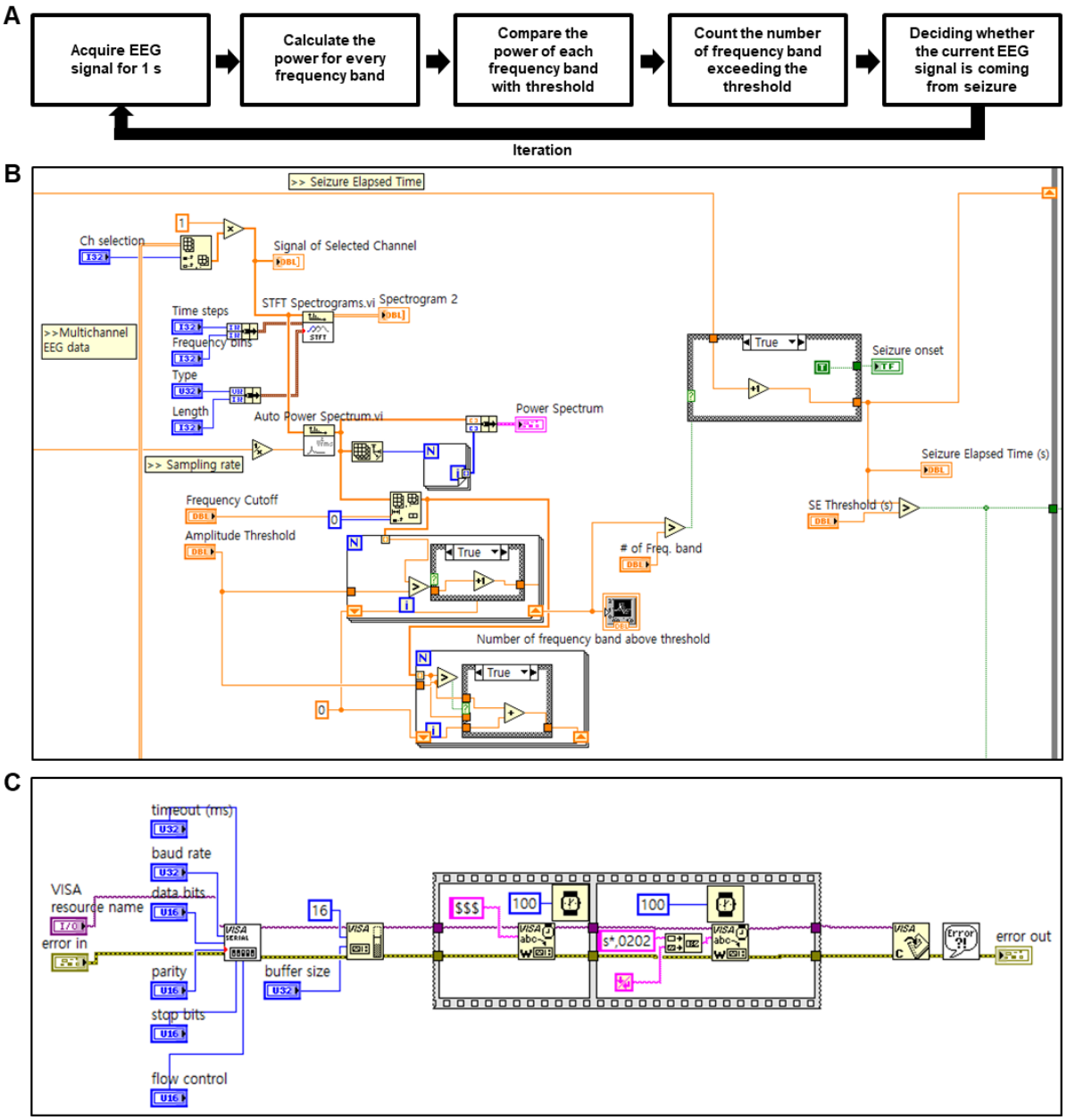

Fig. S20. Detailed explanation of the source code. (**A**) Necessary steps for detecting the seizure signal from the EEG measurement data. (**B**) Detailed source code for the seizure detection and measurement of the time duration of the continuous seizure. (**C**) Detailed source code for the wireless triggering of the subcutaneous drug release from the SID.

SUPPLEMENTARY MOVIES

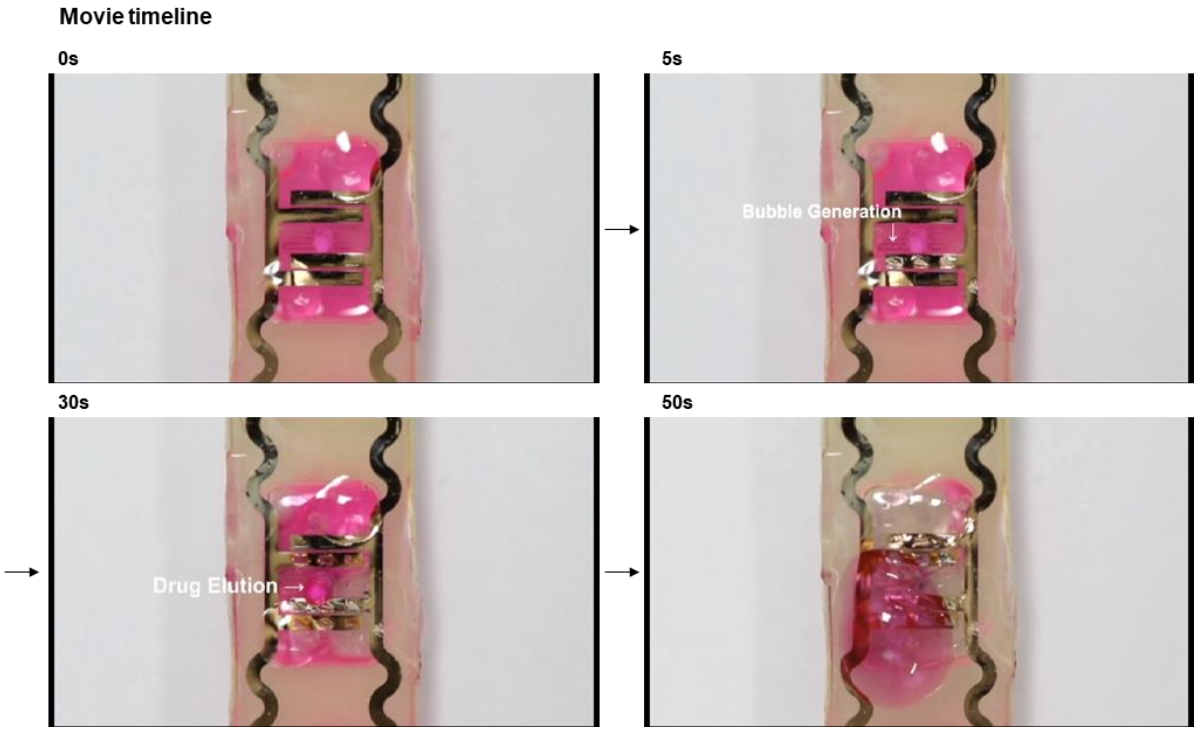

Movie S1. Drug release from SID. Movie showing the bubble generation by water electrolysis and the resulting drug release from the SID.

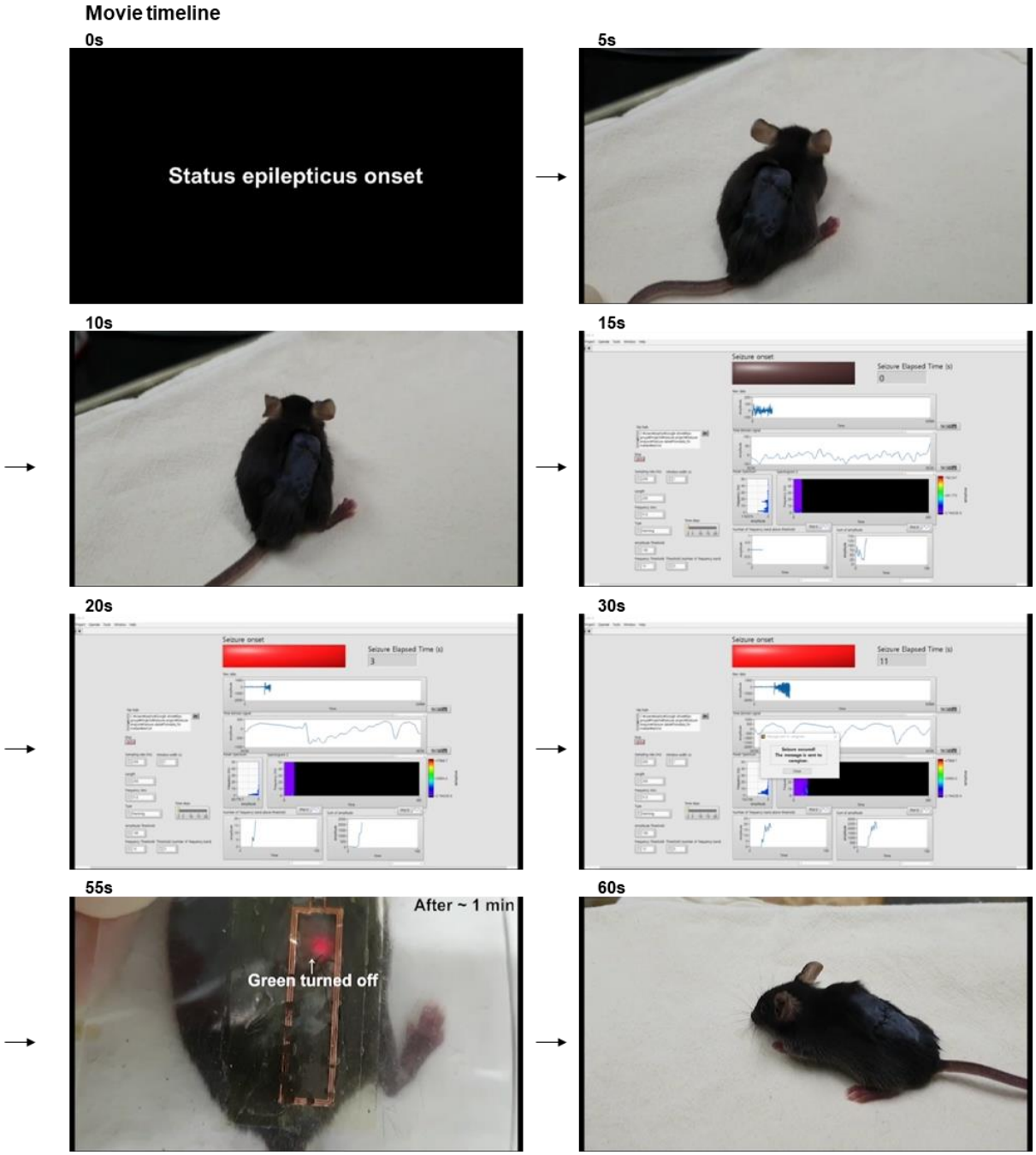

Movie S2. System demonstration. Movie describing the overall system operation.

SUPPLEMENTARY TEXTS

Text S1. Wireless voltage induction

The optimization problem is formulated as follows. The receiver coil size is 20 × 4 mm to fully exploit the SID size, placed beneath the skin layer (z_f= 2 mm distance apart from the source) with its norm in $\hat{z}$–direction (fig. S8A). Human tissues are modeled as a multilayered medium, in which the thickness of the layers are nominally given as (air, skin, fat, muscle, and bone) = (1, 1, 2, 13, 15) in millimeters (fig. S8B). The dielectric permittivity is assigned to each layer from Debye tissue model (*50*). We optimized the current $\boldsymbol{J}_s$ in the source plane to induce the maximum voltage across the receiver coil with a given power dissipated in a lossy human tissue. In a mathematical formulation, it is equivalent to find the current distribution that maximizes the efficiency defined in the main text.

The electric field $\mathbf{E}(\mathbf{r})$ and the magnetic flux density $\mathbf{B}(\mathbf{r})$ can be found from the current sheet $\mathbf{J_s}(\mathbf{r}')$ using the Green's functions, $\mathbf{G}_E(\mathbf{r},\mathbf{r}')$ and $\mathbf{G}_B(\mathbf{r},\mathbf{r}')$, respectively. With the bra-ket notation, $\mathbf{E}$, $\mathbf{B}$, and $\mathbf{J_s}$ can be represented by functions $|\psi\rangle$, $|\phi\rangle$, and $|\xi\rangle$, respectively (*1*, *2*). In this operator formalism, we have $|\psi\rangle = \hat{G}_E|\xi\rangle$ and $|\phi\rangle = \hat{G}_B|\xi\rangle$, where operators $\hat{\Lambda}$ to deduce the change rate of the magnetic flux through the coil area *S* and $\hat{\Sigma}$ to present total dissipative loss in the tissue. Explicitly,

$$\hat{\Lambda}\,|\phi\rangle = \int_S d\mathbf{r}\,\omega\mathbf{B}(\mathbf{r})\cdot\hat{\mathbf{z}} \tag{i}$$

$$\langle\psi|\hat{\Sigma}|\psi\rangle = \int_{tissue} d\mathbf{r}\,\omega\varepsilon''|\mathbf{E}(\mathbf{r})|^2 \tag{ii}$$

Then, the optimization problem of the voltage gain can be re-formulated as a problem that maximizes

$$\eta = \frac{\langle \phi | \hat{\Lambda}^\dagger \hat{\Lambda} | \phi \rangle}{\langle \psi | \hat{\Sigma} | \psi \rangle} = \frac{\left\langle \xi \left| \hat{G}_B^\dagger \hat{\Lambda}^\dagger \hat{\Lambda} \hat{G}_B \right| \xi \right\rangle}{\left\langle \xi \left| \hat{G}_E^\dagger \hat{\Sigma} \hat{G}_E \right| \xi \right\rangle} = \frac{\langle \xi | \hat{A} | \xi \rangle}{\langle \xi | \hat{C}^\dagger \hat{C} | \xi \rangle}$$

where $\hat{A} \coloneqq \hat{G}_B^\dagger \hat{\Lambda}^\dagger \hat{\Lambda} \hat{G}_B$ and $\hat{C}^\dagger \hat{C}$ is the Cholesky decomposition of the Hermitian positive-definite operator $\hat{G}_E^\dagger \hat{\Sigma} \hat{G}_E$. The solution $|\xi_{opt}\rangle$ that maximizes η can be obtained from the eigenvector v_{opt} that satisfies $\hat{C}^{\dagger -1} \hat{A} \hat{C}^{-1} |v_{opt}\rangle = \lambda_{max} |v_{opt}\rangle$ as $|\xi_{opt}\rangle = \hat{C}^{\dagger -1} |v_{opt}\rangle$.

The numerical computation and optimization are performed in plane-wave basis, which are the eigenfunctions of the Green's function operator for the multilayer structure (*35, 51*). As numerical examples, under operating frequencies of 2.5, 40, and 640 MHz, the optimal current sources $|\xi_{opt}\rangle$ are presented in the angular spectrum domain as shown in fig. S7A. The white circles in fig. S7A have the radii of the wavenumber of medium, which is dominantly muscle in this case. Because the receiver coil is only 2 mm apart from the transmit source, most waves are excited in evanescent modes, $k_x^2 + k_y^2 \gg Re(k_{medium})^2$. Evanescent waves efficiently maximize the induced voltage at closely located receiver while minimizing the electric fields elsewhere.

The 2-dimensional Fourier transform of the optimal profiles in plane-wave basis yield those in spatial domain (fig. S7B). The optimal profiles clearly resemble the circulating electric current over similar dimension as the receiver coil for all the selected frequencies. Therefore, the coil structure with comparable size to the receiver coil, which is prevalently used for inductive coupling, is indeed optimal to induce the maximum voltage on the receiver in the near-field region.

Text S2. Wearable sensor and power transmitter

Fig. S3 B to D show the block diagrams of the electronic circuits and their wireless integration for the system construction and operation. The wearable electrophysiology sensor unit (figs. S3B and S4) is designed as an 8-channel sensing device with a Bluetooth communication module (*52*) on a flexible PCB to be worn around the head. The EEG signals are collected through the electrodes connected to channels (fig. S4A (i)). The electrostatic discharge (ESD) protection circuit (fig. S4A (ii)) protects the circuits from potential damages by any unexpected high voltage inputs. The collected signals are then conditioned by passive filters (fig. S4A (iii)) to minimize noises. Then the analog EEG signals are converted to digital signals by an analog-to-digital converter (ADC) (ADS1299IPAGR, Texas Instruments Inc., USA; fig. S4A (iv)). A microcontroller unit (MCU) (PIC32MX250F128B-I/SS, Microchip Technology Inc., USA; fig. S4A (v)) processes the acquired data at the sampling rate of 250 Hz and transmits them to external devices via a Bluetooth module (RFduino 22301, RFdigital Corp., USA; fig. S4A (vi)). The MCU is bootloaded with the PICkit™3 in-circuit debugger (Microchip Technology Inc., USA) via programming pins (fig. S4A (vii)). The Bluetooth module is programmed with FTDI cable breakouts and serial pins (fig. S4A (viii)). Fig. S4 B to D show the detailed PCB artwork of the wearable sensor unit, and fig. S4E shows the chipset information.

The wearable power transmitter (figs. S3C and S5) receives the command signal from the portable device, which processes the EEG data wirelessly sent from the sensor unit. The wireless communications are performed via a Bluetooth module (RN42-I, Microchip Technology Inc., USA; fig. S5A (i)). The portable device sends a string ($$$) that makes the Bluetooth module on the wearable power transmitter to enter the command mode. As the module enters the command mode, the GPIO pins could be controlled externally. The GPIO9 pin is connected to the ON/OFF pin of the 5 V regulator (fig. S5A (ii)), which provides power

to the VCO (CVCO55CL-0038-0042, Crystek Corporation®, USA; fig. S5A (iii)) and the RF amplifier (BGA3023, NXP Semiconductors N. V., Netherlands; fig. S5A (iv)). By turning the GPIO9 pin to the 'high' state, a RF signal with the frequency of 40 MHz is generated. GPIO10 pin is connected to the control pin of the RF switch (PE42724A-Z, pSemi, USA; fig. S5A (v)). By switching between the 'high' and 'low' state of the control pin input, high power RF signals for drug release can be sent directly to the transmit antenna (fig. S5A (vi)) or low power RF signals for device alignment can be sent after bypassing the attenuator (fig. S5A (vii)). The generated RF signal is transmitted by the transmit antenna and provides power wirelessly to the SID. Because LED indicators of the SID should be observed from outside, the transmit antenna was fabricated separately on a transparent PDMS substrate for the see-through design. Fig. S5B shows the entire power transmitter device. The housing of the PCB board was fabricated by a 3D printer (Objet30 Pro, Stratasys Ltd., USA), and a watch silicon strap taken from Samsung Galaxy watch (ET-YSU81MBEGKR, Samsung, South Korea) was used. Fig. S5C shows the chipset information, and fig. S5 D to F show the detailed PCB artwork of the wearable power transmitter.

Text S3. Finite element analysis of SID with mechanical deformation

The strain distribution across the SID is studied with finite element analysis (FEA) by using commercial software (ABAQUS). To reduce computational cost, a 3D half-model is employed to describe the device as illustrated in fig. S15. To be specific, the reservoir is modeled as eight-node linear brick, hybrid elements (C3D8H) with a hyper-elastic material. Four-node shell elements (S4) and eight-node brick elements (C3D8) are used to represent the bottom and the top SU-8 layer, respectively, with the material property. $\mathrm{E} = 2\ \mathrm{GPa}, \nu = 0.22$. For a hyper-elastic material, Ogden model (*53*) with third-order strain energy potential is

employed with coefficients $\mu_1 = 16.9\ kPa, \mu_2 = 0.08\ kPa, \mu_3 = 1.0\ kPa, \alpha_1 = 1.3, \alpha_2 = 5.0, \alpha_3 = -2.0, D_1 = 1.156, D_2 = 0.0001, D_3 = 0$. For the bending simulation, the device is bent until its radius of curvature is decreased up to 1.89 mm, which is beyond the experimentally applied minimum radius of 2 mm. For the pressing test in fig. S14, the SID was embedded between a layer of porcine skin and that of porcine neck tissue, which were modeled as eight-node linear brick elements (C3D8) with $E_{skin} = 5.87\ MPa, \nu_{skin} = 0.49, E_{tissue} = 129.3\ kPa, \nu_{tissue} = 0.49$. The test is performed by applying the pressure up to 40 kPa on the porcine skin. We also varied the thickness of the porcine skin to account for differences of the skin thickness. To consider large deformation, geometric nonlinearity is considered for both simulations.

The FEA results are displayed in Fig. 4, (C and D) and fig. S15. The simulation results in Fig. 4C and fig. S15A reveal that although the reservoir is deformed significantly (e.g., up to 70%, bent to a bending radius of 1.89 mm), the lid made of SU-8 (and the fuse made of gold) experiences a maximum strain of 1.62%. The maximum strain in SU-8 is found to be 1.47%, when the SID was bent to a bending radius of 1.96 mm. Taking the critical strain for rupture of SU-8 to be 1.6%, we can find out that the resistance in the gold fuse exhibited negligible changes during the bending test down to a radius of 2 mm. The simulation for pressing in Fig. 4D reveals that the SID implanted under the thicker skin experiences the less strain when subjected to the same amount of the pressure. The strain distribution of the SID embedded beneath the 1 mm-thick porcine skin is presented in fig. S15B. The maximum strain is found in the gold fuse, where the film of SU-8 is thinnest. At the pressure of 20 kPa and 23 kPa, the maximum strain is 1.42% and 1.60%, respectively. This finding is consistent with the pressing test results shown in Fig. 4B in that the resistance of the gold fuse did not change up to a pressure of 20 kPa.

Text S4. Custom-made software for detection of status epilepticus and wireless triggering of drug release

In order to detect seizure and SE, the software should be able to acquire the EEG signals from the wearable EEG sensor, distinguish the seizure from the normal EEG data in real-time, count the elapsed time of seizure, and wirelessly trigger the wearable power transmitter once the seizure turns into the SE for the elapsed time to exceed the designated threshold (5 min). Fig. S17 A and B show the front panel and block diagram (source code) of the software written with LabVIEW. Once the software starts to wirelessly acquire time series the EEG data from the selected channel, the front panel of the software displays not only the measured EEG data, but also the real-time analysis results of frequency components which are key references to discriminate seizure from the normal EEG data. The software also measures the total duration of time for which the seizure lasts to determine if the seizure develops into the SE. If the seizure lasts longer than the designated period of time (5 min), the software will float a dialogue window to let the user know that the wireless power transmitter will be triggered in designated delay time (right inset of fig. S18A). The user can abort triggering of the power transmitter at this moment if the situation is not urgent. If the designated delay time goes without any responses from the user, the software wirelessly conveys the command signal to the wireless power transmitter to send RF power to the SID wirelessly and thus release the drug from the SID. Movie S2 shows how the software operates the system when the seizure is detected.

For such software operation, source codes were custom-made (fig. S18B). All source codes were written with LabVIEW (National Instruments Corporation, USA). In the initialization step, critical parameters for measurement of the EEG, such as a baud rate, COM port, channels to be used, and grounding information, are wirelessly transferred to the wearable

EEG sensor before the measurement. The users can check whether the intended parameters are correctly set by checking the console panel. The cut-off frequency and order of band-pass and band-stop filters in the software are also adjustable. Fig. S20A shows the process of seizure detection, and fig. S19B shows the enlarged view of the source code related to the seizure detection and measurement of the duration of seizure. The filtered EEG data is analyzed via the fast Fourier transform (FFT) algorithm. The power spectrum could be computed by using the results of FFT for every single frequency band. The power of high frequency components (> 10 Hz) in the EEG signal increased significantly when seizure occurs, whereas it decreased under the normal condition. Therefore, the number of frequency bands whose power is larger than a certain threshold was used as a criterion to judge between the seizure and normal EEG. In particular, if the 1 s long EEG signal contains over 5 frequency bands whose power is over than 5×10^{-12}, the software will consider the EEG data as a seizure signal in mice. The reliability of the seizure detection was investigated by using EEG data from 13 patients that include 32 seizure events. The results show that 90.6% of total event was successfully detected with a positive predictive value of 77.8%. Future studies that employ commercial software and algorithms used in the industry are needed to improve the reliability of the detection.

Once the seizure is detected, the software starts to measure the time duration of the seizure, while it continues to analyze the EEG signal that was obtained for the next 1 s. When the duration of seizure exceeds 5 min, the source code shown in fig. S19C will be executed to trigger the drug release. Once this code is executed, the software will convey the command of "$$$" to the Bluetooth module in the wearable power transmitter to get into the command mode and the command of "s*,0202" to activate GPIO9 of the Bluetooth module to turn on the wearable power transmitter.

REFERENCES AND NOTES

1. D. Khodagholy, T. Doublet, P. Quilichini, M. Gurfinkel, P. Leleux, A. Ghestem, E. Ismailova, T. Hervé, S. Sanaur, C. Bernard, G. G. Malliaras, In vivo recordings of brain activity using organic transistors. *Nat. Commun.* **4**, 1575 (2013).

2. C. Choi, M. K. Choi, S. Liu, M. S. Kim, O. K. Park, C. Im, J. Kim, X. Qin, G. J. Lee, K. W. Cho, M. Kim, E. Joh, J. Lee, D. Son, S.-H. Kwon, N. L. Jeon, Y. M. Song, N. Lu, D.-H. Kim, Human eye-inspired soft optoelectronic device using high-density MoS2-graphene curved image sensor array. *Nat. Commun.* **8**, 1664 (2017).

3. S. Choi, S. I. Han, D. Jung, H. J. Hwang, C. Lim, S. Bae, O. K. Park, C. M. Tschabrunn, M. Lee, S. Y. Bae, J. W. Yu, J. H. Ryu, S.-W. Lee, K. Park, P. M. Kang, W. B. Lee, R. Nezafat, T. Hyeon, D.-H. Kim, Highly conductive, stretchable and biocompatible Ag–Au core–sheath nanowire composite for wearable and implantable bioelectronics. *Nat. Nanotechnol.* **13**, 1048–1056 (2018).

4. C. M. Boutry, L. Beker, Y. Kaizawa, C. Vassos, H. Tran, A. C. Hinckley, R. Pfattner, S. Niu, J. Li, J. Claverie, Z. Wang, J. Chang, P. M. Fox, Z. Bao, Biodegradable and flexible arterial-pulse sensor for the wireless monitoring of blood flow. *Nat. Biomed. Eng.* **3**, 47–57 (2019).

5. M. Kaltenbrunner, T. Sekitani, J. Reeder, T. Yokota, K. Kuribara, T. Tokuhara, M. Drack, R. Schwödiauer, I. Graz, S. Bauer-Gogonea, S. Bauer, T. Someya, An ultra-lightweight design for imperceptible plastic electronics. *Nature* **499**, 458–463 (2013).

6. G. Schwartz, B. C.-K. Tee, J. Mei, A. L. Appleton, D. H. Kim, H. Wang, Z. Bao, Flexible polymer transistors with high pressure sensitivity for application in electronic skin and health monitoring. *Nat. Commun.* **4**, 1859 (2013).

7. D. Son, J. Lee, S. Qiao, R. Ghaffari, J. Kim, J. E. Lee, C. Song, S. J. Kim, D. J. Lee, S. W. Jun, S. Yang, M. Park, J. Shin, K. Do, M. Lee, K. Kang, C. S. Hwang, N. Lu, T. Hyeon, D.-H. Kim, Multifunctional wearable devices for diagnosis and therapy of movement disorders. *Nat. Nanotechnol.* **9**, 397–404 (2014).

8. J. Kim, R. Ghaffari, D.-H. Kim, The quest for miniaturized soft bioelectronic devices. *Nat. Biomed. Eng.* **1**, 0049 (2017).

9. C. M. Proctor, A. Slézia, A. Kaszas, A. Ghestem, I. del Agua, A.-M. Pappa, C. Bernard, A. Williamson, G. G. Malliaras, Electrophoretic drug delivery for seizure control. *Sci. Adv.* **4**, eaau1291 (2018).

10. H. Lee, T. K. Choi, Y. B. Lee, H. R. Cho, R. Ghaffari, L. Wang, H. J. Choi, T. D. Chung, N. Lu, T. Hyeon, S. H. Choi, D.-H. Kim, A graphene-based electrochemical device with thermoresponsive microneedles for diabetes monitoring and therapy. *Nat. Nanotechnol.* **11**, 566–572 (2016).

11. K. Kaszala, K. A. Ellenbogen, Device sensing. *Circulation* **122**, 1328–1340 (2010).

12. R. Proietti, G. Manzoni, L. Di Biase, G. Castelnuovo, L. Lombardi, C. Fundarò, N. Vegliante, G. Pietrabissa, P. Santangeli, R. A. Canby, A. Sagone, M. Viecca, A. Natale, Closed loop stimulation is effective in improving heart rate and blood pressure response to

mental stress: Report of a single-chamber pacemaker study in patients with chronotropic incompetent atrial fibrillation. *Pacing Clin. Electrophysiol.* **35**, 990–998 (2012).

13. J. S. Ho, A. J. Yeh, E. Neofytou, S. Kim, Y. Tanabe, B. Patlolla, R. E. Beygui, A. S. Y. Poon, Wireless power transfer to deep-tissue microimplants. *Proc. Natl. Acad. Sci. U.S.A.* **111**, 7974–7979 (2014).

14. D. R. Agrawal, Y. Tanabe, D. Weng, A. Ma, S. Hsu, S.-Y. Liao, Z. Zhen, Z.-Y. Zhu, C. Sun, Z. Dong, F. Yang, H. F. Tse, A. S. Y. Poon, J. S. Ho, Conformal phased surfaces for wireless powering of bioelectronic microdevices. *Nat. Biomed. Eng.* **1**, 0043 (2017).

15. C. Cobelli, E. Renard, B. Kovatchev, Artificial pancreas: Past, present, future. *Diabetes* **60**, 2672–2682 (2011).

16. F. J. Doyle, L. M. Huyett, J. B. Lee, H. C. Zisser, E. Dassau, Closed-loop artificial pancreas systems: Engineering the algorithms. *Diabetes Care* **37**, 1191–1197 (2014).

17. R. Farra, N. F. Sheppard, L. McCabe, R. M. Neer, J. M. Anderson, J. T. Santini, M. J. Cima, R. Langer, First-in-human testing of a wirelessly controlled drug delivery microchip. *Sci. Transl. Med.* **4**, 122ra21 (2012).

18. K. N. Noh, S. Il Park, R. Qazi, Z. Zou, A. D. Mickle, J. G. Grajales-Reyes, K.-I. Jang, R. W. Gereau, J. Xiao, J. A. Rogers, J.-W. Jeong, Miniaturized, battery-free optofluidic systems with potential for wireless pharmacology and optogenetics. *Small* **14**, 1702479 (2018).

19. Y. Zhang, D. C. Castro, Y. Han, Y. Wu, H. Guo, Z. Weng, Y. Xue, J. Ausra, X. Wang, R. Li, G. Wu, A. Vázquez-Guardado, Y. Xie, Z. Xie, D. Ostojich, D. Peng, R. Sun, B. Wang, Y. Yu, J. P. Leshock, S. Qu, C.-J. Su, W. Shen, T. Hang, A. Banks, Y. Huang, J. Radulovic, P. Gutruf, M. R. Bruchas, J. A. Rogers, Battery-free, lightweight, injectable microsystem for in vivo wireless pharmacology and optogenetics. *Proc. Natl. Acad. Sci. U.S.A.* **116**, 21427–21437 (2019).

20. Y. Zhang, A. D. Mickle, P. Gutruf, L. A. McIlvried, H. Guo, Y. Wu, J. P. Golden, Y. Xue, J. G. Grajales-Reyes, X. Wang, S. Krishnan, Y. Xie, D. Peng, C.-J. Su, F. Zhang, J. T. Reeder, S. K. Vogt, Y. Huang, J. A. Rogers, R. W. Gereau, Battery-free, fully implantable optofluidic cuff system for wireless optogenetic and pharmacological neuromodulation of peripheral nerves. *Sci. Adv.* **5**, eaaw5296 (2019).

21. A. D. Mickle, S. M. Won, K. N. Noh, J. Yoon, K. W. Meacham, Y. Xue, L. A. McIlvried, B. A. Copits, V. K. Samineni, K. E. Crawford, D. H. Kim, P. Srivastava, B. H. Kim, S. Min, Y. Shiuan, Y. Yun, M. A. Payne, J. Zhang, H. Jang, Y. Li, H. H. Lai, Y. Huang, S.-I. Park, R. W. Gereau, J. A. Rogers, A wireless closed-loop system for optogenetic peripheral neuromodulation. *Nature* **565**, 361–365 (2019).

22. Y. Ye, J. Yu, D. Wen, A. R. Kahkoska, Z. Gu, Polymeric microneedles for transdermal protein delivery. *Adv. Drug Deliv. Rev.* **127**, 106–118 (2018).

23. R. Qazi, A. M. Gomez, D. C. Castro, Z. Zou, J. Y. Sim, Y. Xiong, J. Abdo, C. Y. Kim, A. Anderson, F. Lohner, S.-H. Byun, B. Chul Lee, K.-I. Jang, J. Xiao, M. R. Bruchas, J.-W. Jeong, Wireless optofluidic brain probes for chronic neuropharmacology and photostimulation. *Nat. Biomed. Eng.* **3**, 655–669 (2019).

24. J. Lee, H. R. Cho, G. D. Cha, H. Seo, S. Lee, C. Park, J. W. Kim, S. Qiao, L. Wang, D. Kang, T. Kang, T. Ichikawa, J. Kim, H. Lee, W. Lee, S. Kim, S. Lee, N. Lu, T. Hyeon, S. H. Choi, D. Kim, Flexible, sticky, and biodegradable wireless device for drug delivery to brain tumors. *Nat. Commun.* **10**, 5205 (2019).

25. A. Kumar, J. Pillai, *Nanostructures for the Engineering of Cells, Tissues and Organs* (Elsevier, 2018), pp. 473–511.

26. T. H. Blackwell, J. S. Kaufman, Response time effectiveness: Comparison of response time and survival in an urban emergency medical services system. *Acad. Emerg. Med.* **9**, 288–295 (2002).

27. G. M. Brophy, R. Bell, J. Claassen, B. Alldredge, T. P. Bleck, T. Glauser, S. M. LaRoche, J. J. Riviello, L. Shutter, M. R. Sperling, D. M. Treiman, P. M. Vespa, Guidelines for the evaluation and management of status epilepticus. *Neurocrit. Care.* **17**, 3–23 (2012).

28. E. Trinka, H. Cock, D. Hesdorffer, A. O. Rossetti, I. E. Scheffer, S. Shinnar, S. Shorvon, D. H. Lowenstein, A definition and classification of status epilepticus – Report of the ILAE task force on classification of status epilepticus. *Epilepsia* **56**, 1515–1523 (2015).

29. F. Al-Mufti, J. Claassen, Neurocritical care. *Crit. Care Clin.* **30**, 751–764 (2014).

30. Y. W. Wu, D. W. Shek, P. A. Garcia, S. Zhao, S. C. Johnston, Incidence and mortality of generalized convulsive status epilepticus in California. *Neurology* **58**, 1070–1076 (2002).

31. B. K. Alldredge, A. M. Gelb, S. M. Isaacs, M. D. Corry, F. Allen, S. Ulrich, M. D. Gottwald, N. O'Neil, J. M. Neuhaus, M. R. Segal, D. H. Lowenstein, A comparison of lorazepam, diazepam, and placebo for the treatment of out-of-hospital status epilepticus. *N. Engl. J. Med.* **345**, 631–637 (2001).

32. P. Sirikarn, P. Pattanittum, K. Sawanyawisuth, S. Tiamkao, Causes of death in patients with status epilepticus. *Epilepsy Behav.* **101**, 106372 (2019).

33. E. Trevathan, C. C. Murphy, M. Yeargin-Allsopp, Prevalence and descriptive epidemiology of lennox-gastaut syndrome among Atlanta children. *Epilepsia* **38**, 1283–1288 (1997).

34. Y. W. Wu, J. Sullivan, S. S. McDaniel, M. H. Meisler, E. M. Walsh, S. X. Li, M. W. Kuzniewicz, Incidence of dravet syndrome in a US population. *Pediatrics* **136**, e1310–e1315 (2015).

35. S. Kim, J. S. Ho, A. S. Y. Y. Poon, Midfield wireless powering of subwavelength autonomous devices. *Phys. Rev. Lett.* **110**, 203905 (2013).

36. Food and Drug Administration, *Criteria for Significant Risk Investigations of Magnetic Resonance Diagnostic Devices - Guidance for Industry and Food and Drug Administration Staff* (2008); available at www.fda.gov/regulatory-information/search-fda-guidance-documents/criteria-significant-risk-investigations-magnetic-resonance-diagnostic-devices-guidance-industry-and).

37. IEEE Standard for Safety Levels with Respect to Human Exposure to Electric, Magnetic, and Electromagnetic Fields, 0 Hz to 300 GHz, *IEEE* (2019),

doi:10.1109/IEEESTD.2019.8859679.

38. D.-H. Kim, Y.-S. Kim, J. Wu, Z. Liu, J. Song, H.-S. Kim, Y. Y. Huang, K.-C. Hwang, J. A. Rogers, Ultrathin silicon circuits with strain-isolation layers and mesh layouts for high-performance electronics on fabric, vinyl, leather, and paper. *Adv. Mater.* **21**, 3703–3707 (2009).

39. J. Wu, M. Li, W.-Q. Chen, D.-H. Kim, Y.-S. Kim, Y.-G. Huang, K.-C. Hwang, Z. Kang, J. A. Rogers, A strain-isolation design for stretchable electronics. *Acta Mech. Sinica* **26**, 881–888 (2010).

40. S. Jiguet, M. Judelewicz, S. Mischler, H. Hofmann, A. Bertsch, P. Renaud, SU-8 nanocomposite coatings with improved tribological performance for MEMS. *Surf. Coat. Technol.* **201**, 2289–2295 (2006).

41. W. Löscher, Animal models of epilepsy for the development of antiepileptogenic and disease-modifying drugs. A comparison of the pharmacology of kindling and post-status epilepticus models of temporal lobe epilepsy. *Epilepsy Res.* **50**, 105–123 (2002).

42. G. Curia, D. Longo, G. Biagini, R. S. G. Jones, M. Avoli, The pilocarpine model of temporal lobe epilepsy. *J. Neurosci. Methods* **172**, 143–157 (2008).

43. D. Jeon, K. Chu, S.-T. Lee, K.-H. Jung, K.-M. Kang, J.-J. Ban, S. Kim, J. S. Seo, C.-H. Won, M. Kim, S. K. Lee, J.-K. Roh, A cell-free extract from human adipose stem cells protects mice against epilepsy. *Epilepsia* **52**, 1617–1626 (2011).

44. Y. S. Choi, J. Koo, Y. J. Lee, G. Lee, R. Avila, H. Ying, J. Reeder, L. Hambitzer, K. Im, J. Kim, K. Lee, J. Cheng, Y. Huang, S. Kang, J. A. Rogers, Biodegradable polyanhydrides as encapsulation layers for transient electronics. *Adv. Funct. Mater.* **30**, 2000941 (2020).

45. J. Koo, S. B. Kim, Y. S. Choi, Z. Xie, A. J. Bandodkar, J. Khalifeh, Y. Yan, H. Kim, M. K. Pezhouh, K. Doty, G. Lee, Y.-Y. Chen, S. M. Lee, D. D'Andrea, K. Jung, K. Lee, K. Li, S. Jo, H. Wang, J.-H. Kim, J. Kim, S.-G. Choi, W. J. Jang, Y. S. Oh, I. Park, S. S. Kwak, J.-H. Park, D. Hong, X. Feng, C.-H. Lee, A. Banks, C. Leal, H. M. Lee, Y. Huang, C. K. Franz, W. Z. Ray, M. MacEwan, S.-K. Kang, J. A. Rogers, Wirelessly controlled, bioresorbable drug delivery device with active valves that exploit electrochemically triggered crevice corrosion. *Sci. Adv.* **6**, eabb1093 (2020).

46. A. Omurtag, S. G. A. Baki, G. Chari, R. Q. Cracco, S. Zehtabchi, A. A. Fenton, A. C. Grant, Technical and clinical analysis of microEEG: A miniature wireless EEG device designed to record high-quality EEG in the emergency department. *Int. J. Emerg. Med.* **5**, 35 (2012).

47. S.-T. Lee, D. Jeon, K. Chu, K.-H. Jung, J. Moon, J. Sunwoo, D.-K. Park, H. Yang, J.-H. Park, M. Kim, J.-K. Roh, S. K. Lee, Inhibition of miR-203 reduces spontaneous recurrent seizures in mice. *Mol. Neurobiol.* **54**, 3300–3308 (2017).

48. Y. Lee, K. Hwang, Skin thickness of Korean adults. *Surg. Radiol. Anat.* **24**, 183–189 (2002).

49. P. Oltulu, B. Ince, N. Kokbudak, S. Findik, F. Kilinc, Measurement of epidermis, dermis,

and total skin thicknesses from six different body regions with a new ethical histometric technique. *Turkish J. Plast. Surg.* **26**, 56 (2018).

50. S. Gabriel, R. W. Lau, C. Gabriel, The dielectric properties of biological tissues: III. Parametric models for the dielectric spectrum of tissues. *Phys. Med. Biol.* **41**, 2271–2293 (1996).

51. J. S. Ho, B. Qiu, Y. Tanabe, A. J. Yeh, S. Fan, A. S. Y. Poon, Planar immersion lens with metasurfaces. *Phys. Rev. B* **91**, 125145 (2015).

52. K. W. Cho, S. J. Kim, J. Kim, S. Y. Song, W. H. Lee, L. Wang, M. Soh, N. Lu, T. Hyeon, B.-S. Kim, D.-H. Kim, Large scale and integrated platform for digital mass culture of anchorage dependent cells. *Nat. Commun.* **10**, 4824 (2019).

53. D. Steck, J. Qu, S. B. Kordmahale, D. Tscharnuter, A. Muliana, J. Kameoka, Mechanical responses of Ecoflex silicone rubber: Compressible and incompressible behaviors. *J. Appl. Polym. Sci.* **136**, 47025 (2019).